metals

MDPI

Article

Hydrogen Embrittlement of Ti-Al6-V4 Alloy Manufactured by Laser Powder Bed Fusion Induced by Electrochemical Charging

Michaela Roudnicka [1,*], Zdenek Kacenka [2], Drahomir Dvorsky [1], Jan Drahokoupil [1] and Dalibor Vojtech [2]

[1] Institute of Physics, Czech Academy of Sciences, Na Slovance 1999/2, 182 21 Prague, Czech Republic
[2] Department of Metals and Corrosion Engineering, University of Chemistry and Technology, Technicka 5, 166 28 Prague, Czech Republic; vojtechd@vscht.cz (D.V.)
* Correspondence: roudnicka@fzu.cz

Abstract: The 3D printing of Ti-Al6-V4 alloy is subject to much current investigation, with Laser Beam Powder Bed Fusion (PBF-LB/M) being one of the most applied technologies. Ti-Al6-V4 alloy, despite its great material properties, is susceptible to hydrogen penetration and consequent embrittlement. The level of susceptibility to hydrogen penetration depends on the microstructural state of the alloy. In this work, we compare the effect of electrochemical charging by hydrogen on Ti-Al6-V4 alloy prepared by PBF-LB/M, either in the as-built state or annealed, and conventionally prepared alloy. At the same charging conditions, considerably different hydrogen concentrations were achieved, with the as-built 3D-printed material being the most susceptible. The changes in mechanical properties are discussed in relation to changes in microstructure, studied using microscopy, X-ray, and electron diffraction techniques.

Keywords: hydrogen; hydrogen trapping; titanium; Ti-Al6-V4; 3D printing; laser beam powder bed fusion

Citation: Roudnicka, M.; Kacenka, Z.; Dvorsky, D.; Drahokoupil, J.; Vojtech, D. Hydrogen Embrittlement of Ti-Al6-V4 Alloy Manufactured by Laser Powder Bed Fusion Induced by Electrochemical Charging. *Metals* **2024**, *14*, 251. https://doi.org/10.3390/met14020251

Academic Editor: Thomas Niendorf

Received: 19 January 2024
Revised: 16 February 2024
Accepted: 16 February 2024
Published: 19 February 2024

1. Introduction

Ti-Al6-V4 alloy, which belongs among the wider group of α-β Ti-alloys, is the most used titanium alloy in many industries, such as in the automotive, aviation, and chemical fields. It is also one of the most commonly used biomaterials. The benefits of this alloy are very good mechanical properties at relatively low material density and excellent corrosion properties, even in aggressively corrosive environments [1]. One of the problems with this alloy is titanium susceptibility to hydrogen penetration into the metallic lattice. Hydrogen causes changes in microstructure and subsequently in mechanical properties (hydrogen embrittlement) [2]. As the degree of hydrogen penetration and embrittlement depends on microstructural state, Ti-Al6-V4 alloy can respond differently in different material states [3,4].

Some industrial processes in which hydrogenation occurs are cathodic protection, electrochemical plating, welding, pickling, and exposition in the atmosphere with a high concentration of hydrogen, among others. During these processes, hydrogen penetrates into the metal, diffuses, and either stays in the interstitial positions of the solid solution or reacts with Ti atoms to form hydrides [5]. The formation of brittle hydrides results in decreasing tensile properties in the Ti-Al6-V4 alloy, such as loss of ductility and a reduction in the critical stress intensity factor [3,6].

The microstructure of Ti-Al6-V4 alloy can vary vastly depending on the manufacturing route. Conventional methods to produce this alloy include investment casting or machining and welding. However, low heat conductivity and work-hardening makes titanium machining quite challenging. Moreover, as titanium is a relatively expensive material, large material losses are undesirable. Thus, "near-net-shape" processing is promoted. An unconventional, rapidly developing "near-net-shape" processing method is additive manufacturing (3D printing) based on gradual joining of metal powders into the form

of final products. Components are built layer by layer. Laser Beam Powder Bed Fusion of Metals (PBF-LB/M), one of the most widely used 3D printing technologies, popularly known as Selective Laser Melting (SLM), employs a highly focused laser beam to gradually melt small volumes of source powder according to a precisely defined trajectory derived from the 3D model of the manufactured part [1,4,7].

Specifics of PBF-LB/M, such as high cooling rates, directional cooling and complex thermal history (partial remelting of the solidified material, repeated heat effect), results in specific microstructures of the Ti-Al6-V4 alloy. Moreover, final microstructures may also vary based on the specific parameter setting used in the printing process. Laser power, scanning speed, scanning strategy, layer thickness applied, and many other parameters affect the properties of the melt pool, and therefore the melting/solidification process [8]. Generally, additional heat treatment is applied after printing the Ti-Al6-V4 alloy by PBF-LB/M. High residual stresses increase the risk of damage to the component already when it is being removed from the construction platform, but they also significantly degrade the required mechanical properties of the alloy [9].

Not many studies describing the effect of hydrogen penetration on the mechanical properties of Ti-Al6-V4 alloy manufactured additively are currently available. There are several studies [10–14] dealing with hydrogen trapping in Ti-Al6-V4 alloy prepared via Electron Beam Powder Bed Fusion of Metals (PBF-EB/M), another additive manufacturing technology belonging in the same technological group of powder-bed technologies as PBF-LB/M. However, PBF-EB/M yields a material with a different microstructure than PBF-LB/M due to the use of an electron beam, vacuum, and different fabrication strategy, and thus a different thermal history experienced by the material. A hydrogenation/dehydrogenation process was applied to PBF-LB/M samples by Bilgin et al. [15] as well as Guo et al. [16] to refine the microstructure of the alloy and increase its ductility. Silverstein and Eliezer [17] showed that the susceptibility to hydrogen trapping significantly depends on the printing direction of PBF-LB/M.

In the above-mentioned studies, high-temperature hydrogenation from the gas phase was applied. However, this process yields different transformation mechanisms than electrochemical hydrogenation at room temperature. As material interaction with H occurs in many industrial electrochemical processes applied to process and treat the Ti-Al6-V4 alloy, we focused on this problematics in our study. Only very few similar studies can be found. Wu et al. [3] studied the effect of sample orientation during PBF-LB/M build-up on the susceptibility to hydrogen embrittlement and showed that horizontally built samples (parallel to the building platform) are more prone to hydrogen damage. Deconinck et al. [4], in addition, studied the effect of the as-built surface on the degree of hydrogen uptake. Metalnikov et al. [18] compared hydrogen interactions with Ti-Al6-V4 alloy processed by PBF-LB/M and PBF-EB/M. Different degradation mechanisms were suggested. Navi et al. [14] compared the response of PBF-EB/M samples to electrochemical charging with that of wrought samples and pointed out their higher susceptibility to hydrogen embrittlement due to the specific microstructure despite lower hydrogen uptake.

Our study provides a comprehensive overview of susceptibility to hydrogen penetration and associated interactions in the Ti-Al6-V4 alloy prepared via PBF-LB/M, as compared with the alloy prepared conventionally, including the effect of heat treatment. It develops results briefly reported in a short letter published previously [19], which hinted that 3D-printed samples are twice as susceptible to H absorption as their conventionally manufactured counterpart. Moreover, heat treatment of the 3D-printed samples was shown to partially reduce this susceptibility. The main purpose of this paper is to explain the microstructural changes and severe deterioration of mechanical properties occurring with H-charging in studied materials.

2. Materials and Methods

Changes in microstructure and mechanical properties caused by hydrogen charging were studied in samples printed by PBF-LB/M technology. One group of these samples

was subjected to heat treatment after printing. A third sample group was made via forging, to provide a direct comparison of the 3D printing method with the conventional production of Ti-Al6-V4 alloy. Sample designation is summarized in Table 1.

Table 1. Sample designation.

Sample Designation	Sample Type	Preparation Route
3D	3D-printed by the PBF-LB/M technology	Original as-printed state
3D_H	3D-printed by the PBF-LB/M technology	Original as-printed state, hydrogen-charged
3D + HT	3D-printed by the PBF-LB/M technology	Heat-treated state
3D + HT_H	3D-printed by the PBF-LB/M technology	Heat-treated state, hydrogen-charged
CM	Conventionally manufactured	Original hot-forged state
CM_H	Conventionally manufactured	Hot-forged state, hydrogen-charged

2.1. Sample Preparation

Samples were printed using an M2 Cusing machine (ConceptLaser, Lichtenfels, Germany) from a Ti-6Al-4V powder (CL 41TI ELI, ConceptLaser) with an average particle size of 45 µm. The powder was deposited onto a preheated building platform (200 °C) in layers of 30 µm in thickness. The laser power used was 200 W and the scanning speed was 0.8 m/s. A chessboard printing strategy was applied, with a square size of 5 × 5 mm^2. The scanning direction in adjacent square fields was perpendicular. The hatching distance between adjacent laser traces within one square field was 120 µm. The samples were printed directly in the form of flat dog-bone tensile bodies in the vertical orientation. On one building platform, 30 samples were built at once. As-printed samples were subjected to surface treatment; polishing to a roughness of 1.6 µm in an industrial milling machine. Sample shape and dimensions are given in Figure 1. The relative density of the samples was determined by optical microscopy and image analysis to be 99.7 ± 0.1%.

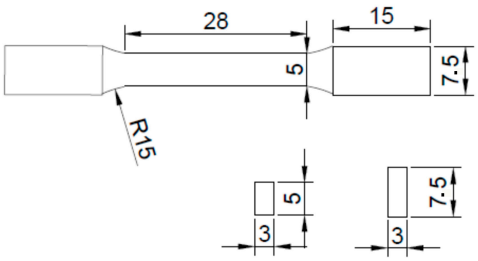

Figure 1. Shape and dimensions (mm) of testing samples.

One-half of the samples were heat treated to remove internal stresses after printing. Samples were subjected to a common stress-relief heat treatment in a vacuum furnace Xerion X'Retort (Xerion Berlin Laboratories® GmbH, Berlin, Germany): heated up at a speed of 200 °C/min to the annealing temperature of 820 °C, annealed for 90 min, and then slowly cooled down in the furnace.

Reference samples of the same dimensions and surface state were machined from a commercially purchased hot-forged bar.

2.2. Hydrogen Charging

Electrochemical hydrogen charging was performed galvanostatically in an electrolyte containing H_3PO_4 and glycerol in a 1:2 ratio. Samples were connected as a cathode, and a platinum net was used as an anode. This two-electrode cell was connected to a programmable switching power supply (DC PSW 160-21.6, GW Instek, Good Will Instrument

Euro B.V., Veldhoven, The Netherlands). The charging was carried out at room temperature for 48 h at a current density of 50 mA/cm^2. Samples were cleaned with distilled water and ethanol in an ultrasonic cleaner after the hydrogen charging. Each sample was charged separately in a freshly prepared electrolyte. Samples were stored in a fridge for the following experiments.

2.3. Material Characterization and Testing

To assess the hydrogen content before and after hydrogen charging, combustion analysis was performed using a G8 Galileo analyzer (Bruker, Billerica, MA, USA). Nitrogen was used as the carrier gas, and calibration was completed using hydrogen gas of 5.0 purity (99.999%). The phase composition was investigated by X-ray diffraction (XRD) using a diffractometer PANalytical X'Pert Pro (Malvern Panalytical, Malvern, UK) in Bragg-Brentano geometry with a Co anode providing K$\alpha_{1,2}$ radiation ($\lambda_{K\alpha1}$ = 1.78901 Å). The first measurement was from the surface. Next, depth profiles of phase composition were constructed by measuring XRD in several subsequent cuts from sample surface towards the center. The effective penetration (ca. 68% of diffracted intensity) depth of the measurement was about 3 μm. The phase composition and lattice parameters were evaluated via the application of the Rietveld refinement [xrd1] method [20] using Topas software (version 3). Due to the complexity of the diffraction patterns, the crystallite size and microstrain parameters were fixed to the same value for measurements of subsequent cuts to stabilize the results of phase analysis. In some cases, the lattice parameters were manually set to reach more physical agreement between measured and calculated diffraction patterns. Metallography cuts were prepared via gradual mechanical grinding on SiC papers of P1000-4000 roughness.

The material microstructure was studied by means of optical (OM) and scanning electron (SEM) microscopy. Microstructure was observed in sections perpendicular to the building direction of PBF-LB/M, or in the forging direction. For optical microscopy (Observer.D1m, Carl Zeiss AG, Jena, Germany), sample sections were prepared via mechanical grinding and polishing with a silica suspension (Eposil F) supplemented with 20 vol% of hydrogen peroxide. Kroll's reagent was used for etching. The same sections were then observed using SEM (Vega-3 LMU, Tescan, Brno, Czech Republic). Surface analysis before and after hydrogen charging was provided through electron dispersion spectroscopy (Oxford Instruments analyzer, Abingdon-on-Thames, UK).

The mechanical properties of the materials were described by tensile tests and by hardness measuring. Tensile tests were carried out on an Instron 5882 universal loading machine (Instron, Norwood, MA, USA) at a constant strain rate of 10^{-3} s^{-1}. At least two tensile specimens for each condition were tested. Fracture surfaces were observed using a scanning electron microscope (Tescan Vega-3 LMU). Vicker´s microhardness (HV0.1, microhardness tester Duramin, Struers GmbH, Roztoky, Czech Republic) was measured on metallography samples in order to create hardness profiles indicating the depth of hydrogen penetration into the microstructure and its affection. The average microhardness value at a particular depth was evaluated from three indentations.

3. Results

3.1. Hydrogen Content

The level of hydrogen content in samples was investigated using combustion analysis. The results are presented in Table 2. All tested samples in the original noncharged state showed a small amount of hydrogen, with the highest value contained in the as-printed sample. After hydrogen charging, the hydrogen content increased significantly in all samples. The highest increase (almost 50 times compared to the noncharged state, and double the value of the charged CM sample) was measured in the as-printed sample. Heat treatment decreased the amount of hydrogen entering the microstructure, but the hydrogen content was still ~30% higher than in the lattice of the conventionally manufactured sample.

Table 2. Hydrogen content in the analyzed samples.

Sample Type	Noncharged	Charged
3D	114 ± 38 ppm	5458 ± 482 ppm
3D + HT	59 ± 40 ppm	3772 ± 52 ppm
CM	41 ± 6 ppm	2857 ± 35 ppm

3.2. Hydrides Analysis

The presence of hydrides was confirmed by the XRD analysis. Because the atomic scattering factor of H is more than 20 times weaker than the atomic scattering factor of Ti, its presence cannot be directly determined using X-ray diffraction. However, how it affects the unit cell size and symmetry can be observed. Figure 2b presents representative XRD patterns for the hydrogenated samples, measured at a depth of 0.12 mm below the sample surface. The thorough evaluation of present phases and their volume fractions throughout the sample depth is then given in Figure 3 for all samples. Two types of hydrides were discovered on the surface of all samples, but also in the sample volumes at a lower concentration. Regarding the similarity of obtained results with the study of Navi et al. [14], we have remained consistent with their notation and designate the hydrides as δ_A and δ_B. The atomic ratios were approximately determined from measured lattice parameters and assigned space groups (Table 3) as TiH1.5 for δ_A-hydride and TiH0.33 for δ_B-hydride. According to our evaluation, diverging from that in Ref. [14], TiH1.5 has a face-centered tetragonal (fct) lattice with a = 4.28 Å and c = 4.36 Å. The atomic ratio was approximated from a theoretical study of Wang and Wang [21], which shows good agreement with experimental results that the TiH_x (x = 0–2) structural stability changes from face-centered cubic (fcc) ($x \leq 0.5$) to fct ($0.75 \leq x \leq 1.5$) and back to fcc ($1.75 \leq x \leq 2$). The second lower-hydrogen hydride TiH0.33 has a cubic (fcc) lattice with NaCl structure and hydrogen occupying interstitial positions. The first mentioned hydride was dominant on the surface and its content gradually decreased towards the sample center. From a depth of approximately 0.3 mm and beyond, its content stabilized at about 2–5 vol%. In the subsurface layer, about 0.1 mm below the surface, the content of the δ_B-hydride locally increased. Similar trends were observed for all sample types (see Figure 3), with slight differences in the absolute amount of present hydrides, probably depending on a particular mechanism of hydrogen ingress into the materials based on the structural differences.

Table 3. Lattice parameters and space groups of the detected phases.

		3D		3D + HT		CM	
Phase	**Space Group**	**a (Å)**	**c (Å)**	**a (Å)**	**c (Å)**	**a (Å)**	**c (Å)**
				Non-hydrogenated state			
α	P 63/m m c	2.93	4.67	2.92	4.68	2.94	4.67
β	I m −3 m			3.19		3.24	
				Hydrogenated state			
α/α_H	P 63/m m c	2.93	4.67–4.69	2.93	4.67–4.69	2.93–2.94	4.67–4.69
β_H	I m −3 m	changing with sample depth, presented in Figure 4					
δ_A	P 42/n S	4.28	4.36	4.28	4.36	4.28–4.31	4.35–4.36
δ_B	F m −3 m	4.1–4.2		4.13–4.14		4.14–4.15	

Apart from the present hydrides, the comparison of XRD diffraction patterns in the charged (Figure 2b) and uncharged (Figure 2a) states showed that β-phase peaks shifted to lower reflection angles compared to the original non-hydrogenated β-phase, indicating an increase in the unit cell size of the β-phase due to hydrogen presence in the body-centered cubic (bcc) solid solution (designated as β_H). The expansion of the lattice parameter of the β_H-phase with the sample depth is depicted graphically in Figure 4. For conventionally manufactured and 3D printed samples with heat treatment, which have an α + β structure, hydrogen diffuses mostly via the β structure and increases its lattice parameter [22]. For the

CM_H sample, the lattice parameter was affected to the depth of 500 µm. In the 3D + HT_H sample, the lattice parameter was increased for all measurements throughout the sample, which indicates that hydrogen diffused throughout the whole thickness of the sample. The amount of β-phase in these samples remained similar to that in the original samples, indicating that the hydrides were transformed from the α-phase. From our measurements, the conversion rate of the α-phase can be estimated to be 45% for the 3D + HT_H samples and 35% for the CM samples, indicating again the higher susceptibility of the 3D printed sample to hydrogen ingress. Almost no shift was registered in the α-phase due to the low solubility of hydrogen in the α-phase [23]. Compared to 3D + HT and CM samples, 3D printed samples without heat treatment had a fully martensitic structure with a high degree of internal stress. XRD showed that, through the action of hydrogen, the hexagonal martensitic phase was partially converted to the β-phase (Figure 3a). The newly formed β_H phase showed a significantly larger lattice parameter (a = 3.35 Å) than the one originally present in other two samples (3D + HT: a = 3.19 Å, CM: a = 3.23 Å), independent of the measurement depth. Most of the β_H phase was formed at a depth of 120 µm, but some was formed throughout the whole sample. Again, this indicates hydrogen diffusion throughout the entire sample.

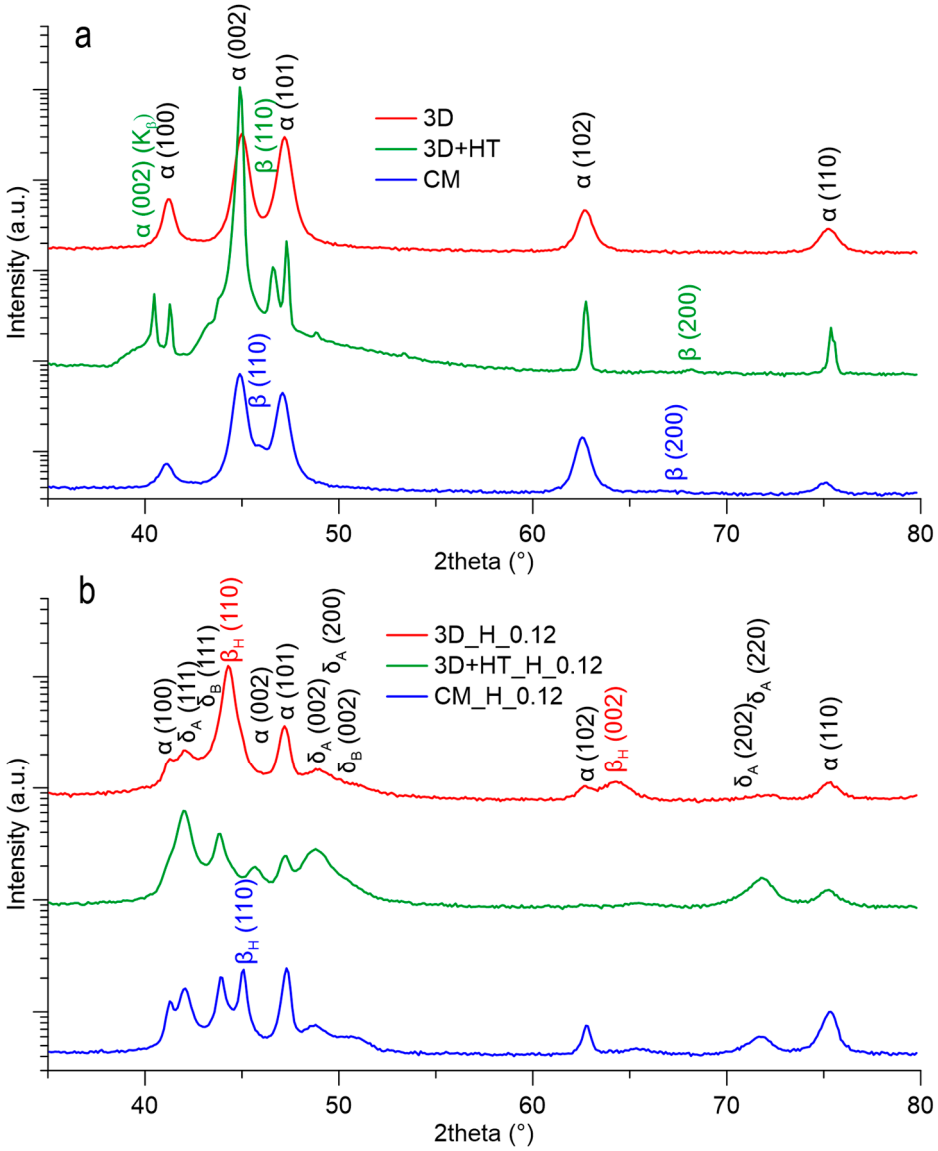

Figure 2. XRD patterns of (**a**) non-hydrogenated and (**b**) hydrogenated samples (Patterns of hydrogenated samples measured at the depth of 0.12 mm.).

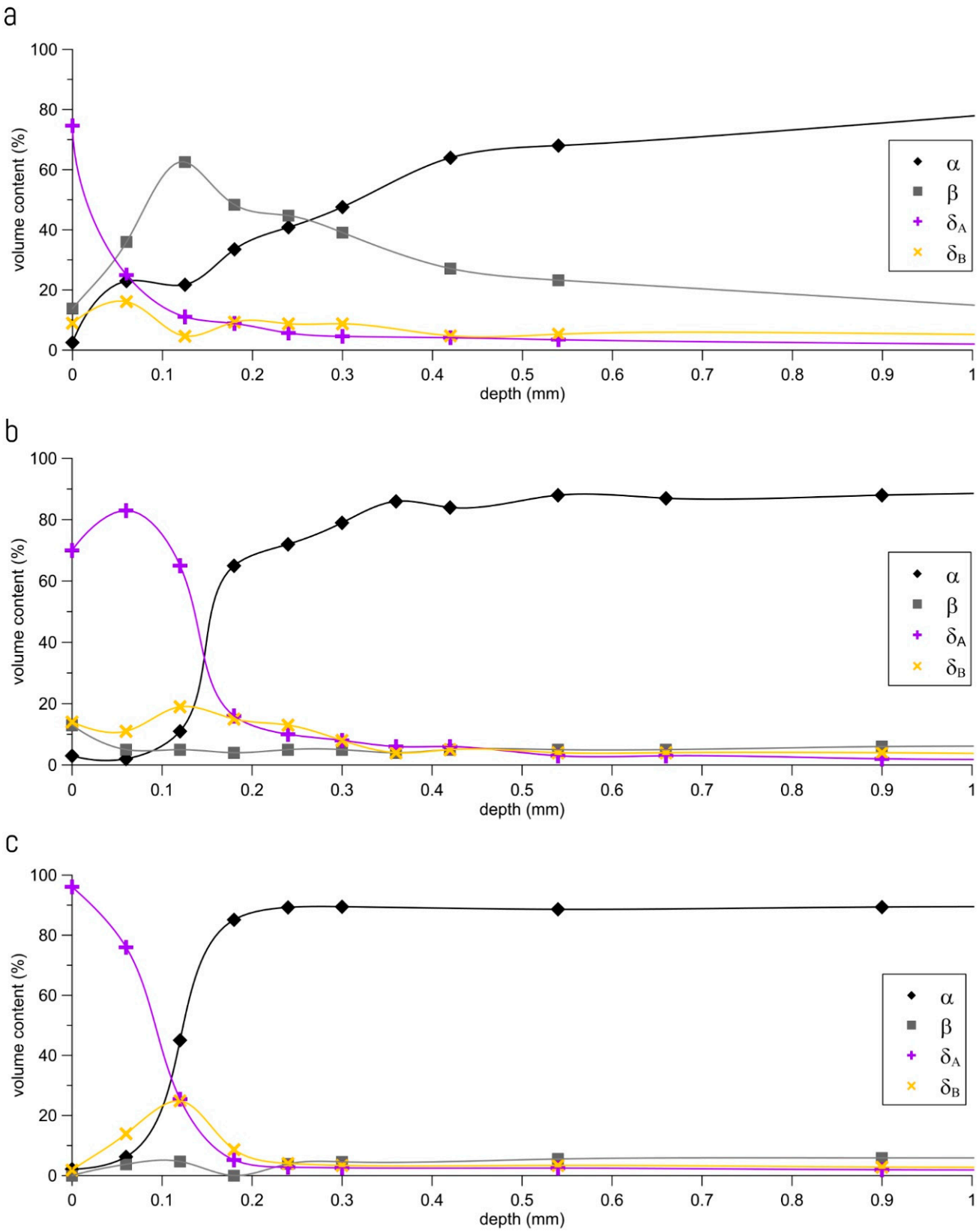

Figure 3. The course of the phase composition throughout the (**a**) 3D_H, (**b**) 3D + HT_H, and (**c**) CM sample.

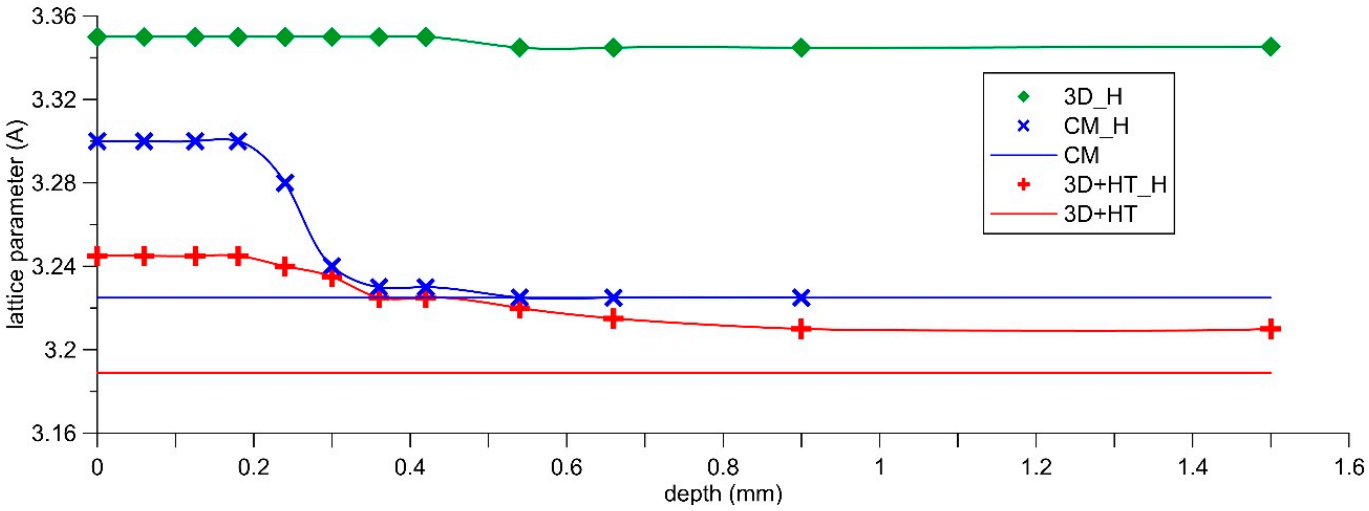

Figure 4. The change of the β-phase lattice parameter with the depth of hydrogenated samples.

3.3. Microstructure

The changes in the microstructures of the charged and non-charged samples were investigated using OM and SEM. Optical micrographs (Figure 5) show the first manifestation of microstructural changes in the surface layer of the samples. A layer of ~335 ± 30 μm in thickness is visible in the 3D + HT sample after H-charging (Figure 5e). A similar layer is present in the conventionally manufactured sample, but it is three times thinner (~110 ± 12 μm) (Figure 5h). The layers are not clearly delimited; there is a transitional area between the surface layer and the sample volume. The influence of H manifested in a different way in the 3D as-built samples. In optical micrographs (Figure 5b,c), the 3D_H sample showed a heavily deformed surface layer to a depth of ~455 ± 35 μm. The depth of the direct influence by H (surface layer thickness) follows the same trend as the determined concentration of H in the samples: 3D_H > 3D + HT_H > CM_H.

SEM images are shown in Figure 6. As-built 3D printed samples show fully martensitic acicular microstructure (Figure 6a). Heat treatment yielded transformation into a two-phase lamellar microstructure; martensitic needles thickened and transformed into lamellae of the α-phase, separated by an interlamellar β-phase (Figure 6d). Conventionally manufactured samples showed stable two-phase microstructure as well, but consisting of equiaxed α-grains with β-phase particles at their boundaries (Figure 6g). A β-phase richer in V and more resistant to etching appears brighter in the micrographs. Both 3D + HT and CM samples contained about 12.5 vol% of β-phase. The microstructural changes after hydrogen charging are depicted in the remaining images of Figure 6, with the second column showing the surface layer of the samples and the third representing the microstructure deeper in the bulk, at a depth of approx. 400 μm. It should be noted that hydrides are difficult to visualize using SEM. However, their predominance in the surface layer of the samples (as detected by XRD) is responsible for the observed changes in the micrographs (due to an altered response to etching). In the 3D_H sample, the acicular microstructure coarsened in the subsurface layer of the sample (Figure 6b). In contrast, the microstructure became relatively homogeneous at a depth of approx. 400 μm (Figure 6c). Similar coarsening occurred in the subsurface layer of 3D + HT_H (Figure 6e) and CM_H samples (Figure 6h). Deeper in the sample, the microstructure remained almost unchanged (Figure 6f,i).

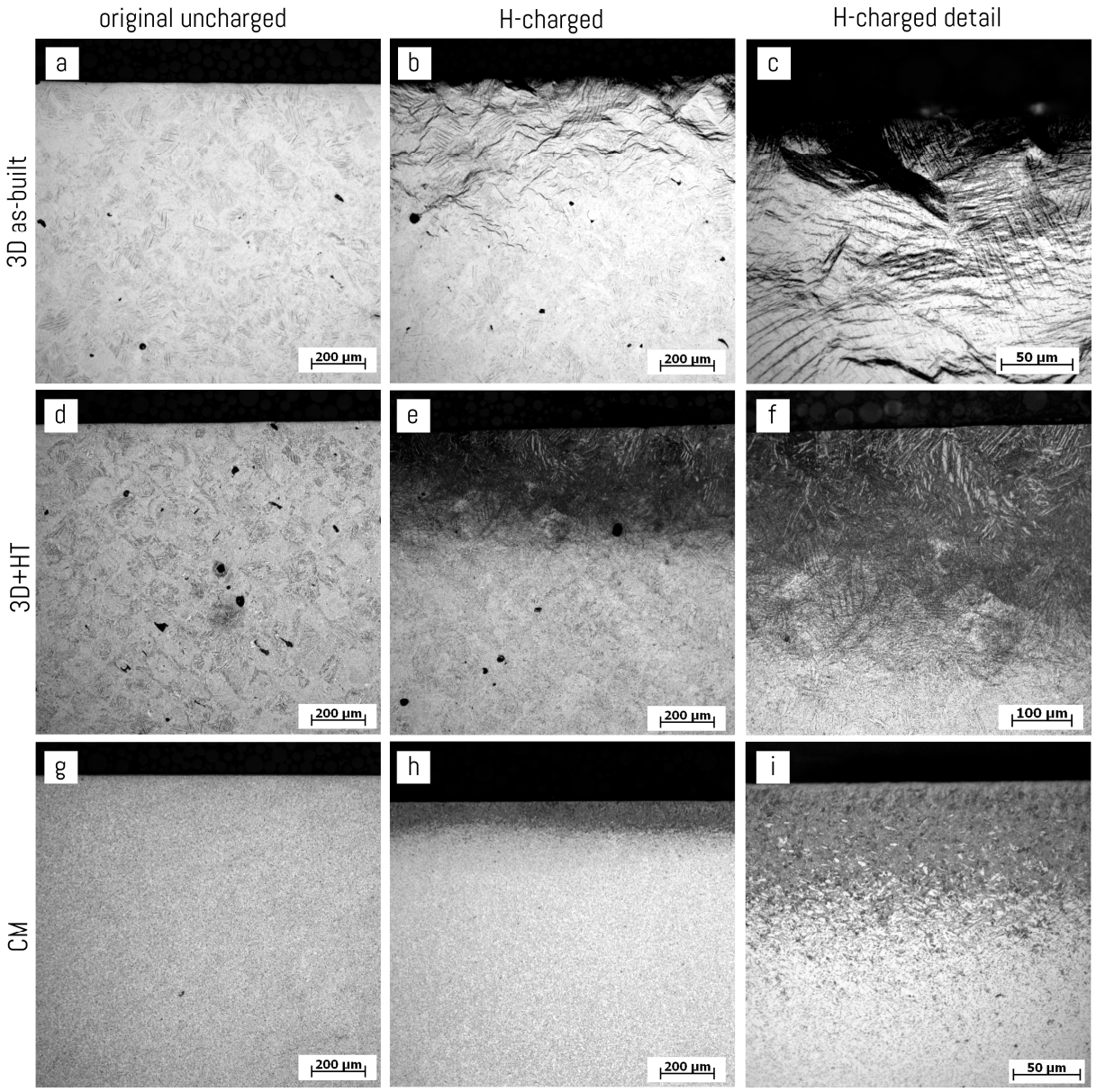

Figure 5. Optical micrographs of the samples showing the changes of the surface layer after H-charging: (**a**) 3D, (**b**,**c**) 3D_H, (**d**) 3D + HT, (**e**,**f**) 3D + HT_H, (**g**) CM, (**h**,**i**) CM_H.

3.4. Changes in Mechanical Properties

3.4.1. Hardness

Microhardness profiles in Figure 7 better reflect the effect of hydrogen in the distinctive microstructures of the tested samples of the Ti-Al6-V4 alloy. While the conventionally manufactured sample (Figure 7c) shows a clear and strong hardness increase in the surface layer of the sample affected by hydrogen, the 3D printed sample without heat treatment (Figure 7a) shows strong softening in the surface layer. Heat treatment of the 3D printed sample almost eliminated the hydrogen influence on hardness (Figure 7b). Hardening was not gradual as in the case of CM sample, but increased hardness values were measured locally at a depth of ~100–150 µm. The hardness increase was also not as strong (18% increase compared to 45%).

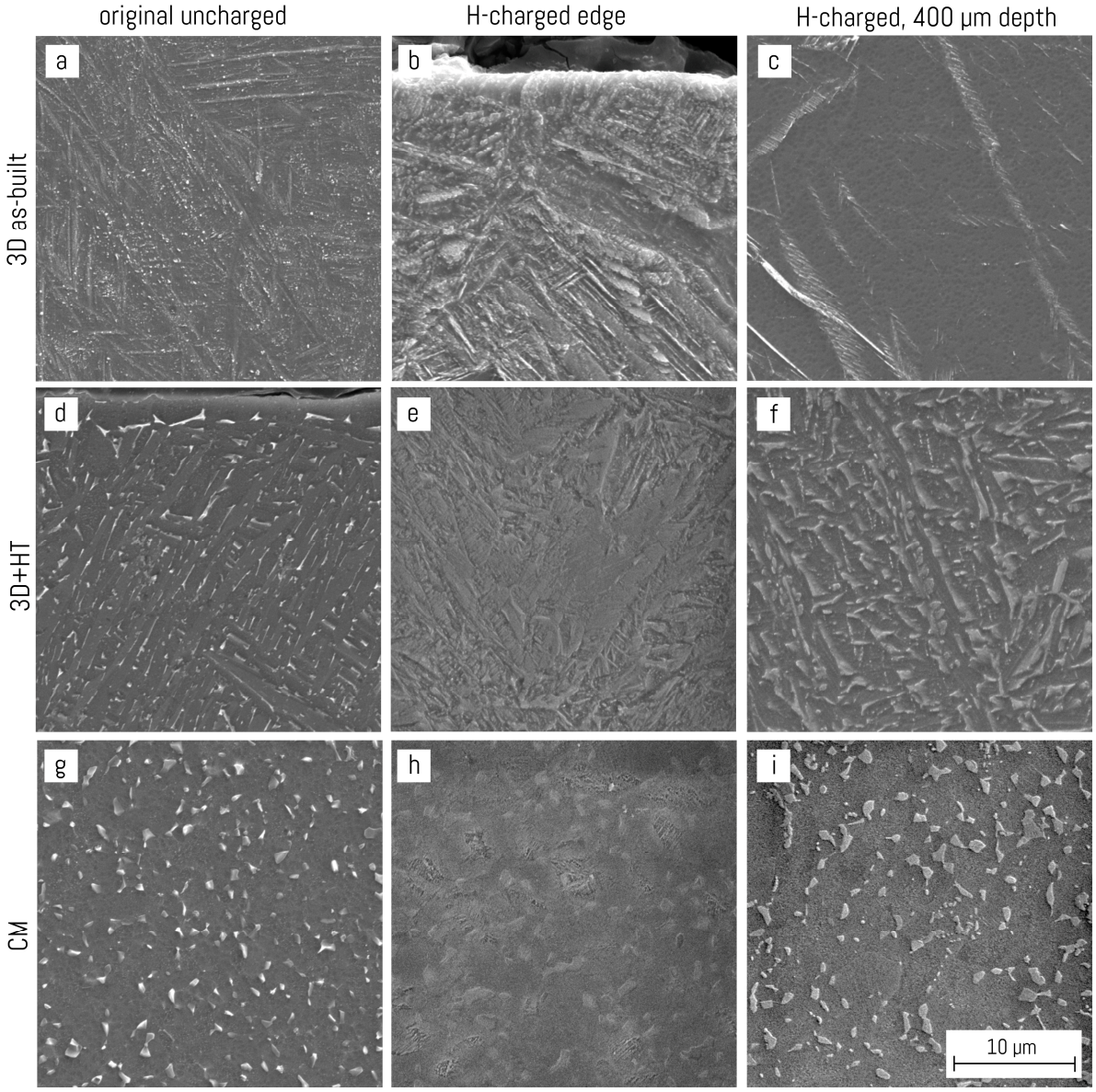

Figure 6. SEM images of analyzed microstructures (same magnification for all images): (**a**) 3D, (**b**,**c**) 3D_H, (**d**) 3D + HT, (**e**,**f**) 3D + HT_H, (**g**) CM, (**h**,**i**) CM_H.

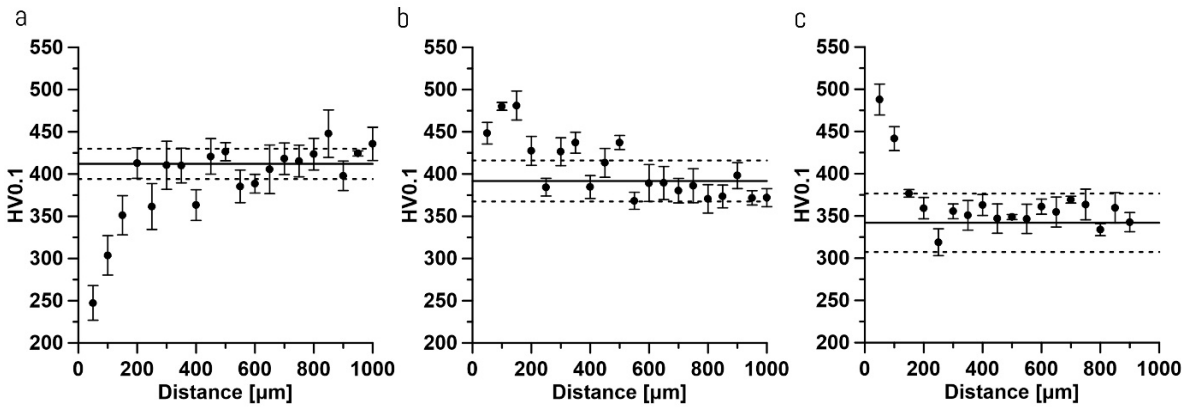

Figure 7. Microhardness profiles of (**a**) 3D_H, (**b**) 3D + HT_H, and (**c**) CM_H samples. The solid line is the average value of the microhardness of the non-hydrogenated samples and the dashed lines represent the standard deviations from this value.

3.4.2. Tensile Testing

The goal of tensile testing was to investigate the effect of hydrogenation on the mechanical properties of the 3D-printed Ti-Al6-V4 samples. Therefore, charged and noncharged samples were measured and compared. Representative tensile curves are plotted in Figure 8 and evaluated mechanical properties are given in Table 4.

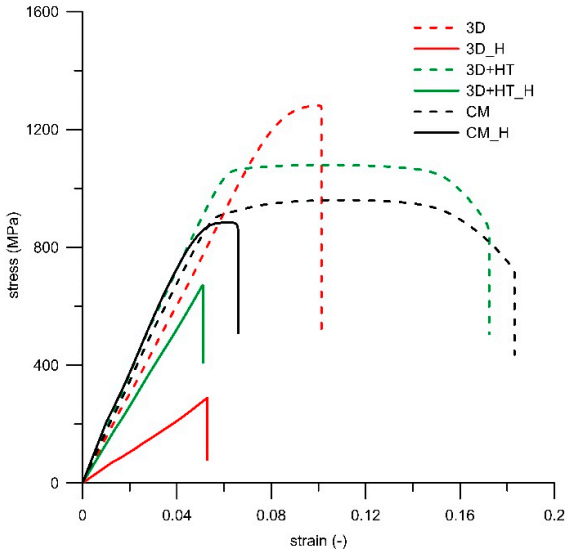

Figure 8. Representative tensile stress-strain curves of hydrogenated and nonhydrogenated samples of Ti-Al6-V4 alloy.

Table 4. Selected mechanical properties in tension.

Sample	Tensile Yield Strength (MPa)	Ultimate Tensile Strength (MPa)	Elongation (%)
3D	1207 ± 10	1263 ± 19	2.1 ± 0.5
3D_H	/	182 ± 11	/
3D + HT	1032 ± 12	1071 ± 8	12.1 ± 0.5
3D + HT_H	/	546 ± 13	/
CM	899 ± 20	975 ± 15	14 ± 0.1

A decrease in both strength and elongation was observed for all types of samples after hydrogen charging. A general trend can be deduced: both strength and ductility decrease with an increasing amount of hydrogen in the material (Table 2). The most severe decrease occurred in the case of the as-built sample without heat treatment with the highest H content. The ultimate tensile strength (UTS) of this material decreased from 1207 MPa to only 182 MPa, and the sample completely lost its ductility. A large drop in both UTS and elongation also occurred for the 3D-printed sample with heat treatment, but it was not as severe as for the sample without heat treatment. For both 3D printed samples, the progress of tensile curves changed with hydrogen charging; the area of plastic deformation of these samples disappeared. Thus, it can be concluded that the samples became completely brittle due to hydrogen charging. The conventionally manufactured sample preserved its strength, and even a partial degree of ductility.

Fractography (fracture surfaces in Figure 9) showed that the brittle behavior stems mainly from the brittle surface layer. After hydrogen charging, fracture morphology changed from ductile to brittle in the surface layer of the samples while it remained fully or partially ductile in the sample volume. The depth of the brittle layer was approximately determined from the fracture surfaces. A clearly defined transition between the brittle surface layer, at about 200 μm in depth, and the dimple-like sample volume was observed in the conventionally manufactured sample. In 3D-printed samples, the transition is less distinct, with some transi-

tional area. The depth of the brittle surface layer was about 400–500 µm and 500–700 µm for the 3D_H and 3D + HT_H samples, respectively. This trend corresponds with metallography observations (Figure 5). No necking occurred for the hydrogen charged samples and the samples cracked perpendicularly to the loading direction.

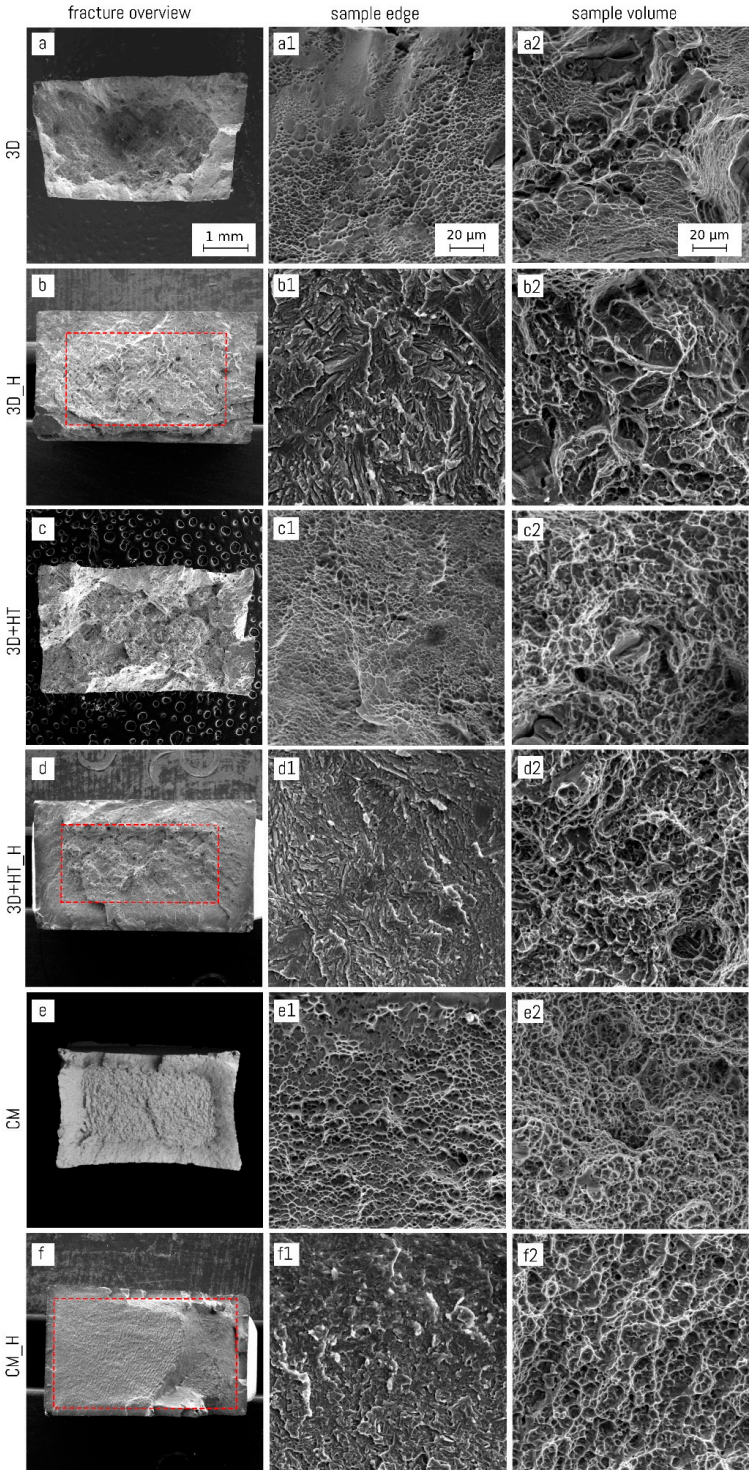

Figure 9. Fracture surfaces of tested samples: (**a**,**a1**,**a2**) 3D, (**b**,**b1**,**b2**) 3D_H, (**c**,**c1**,**c2**) 3D + HT, (**d**,**d1**,**d2**) 3D + HT_H, (**e**,**e1**,**e2**) CM, (**f**,**f1**,**f2**) CM_H. The scale is kept the same for all images in the same column. Subfigures marked with no.1 show sample edge, subfigures marked with no.2 show sample volume. Red dashed-lined boxes in (**b**,**d**,**f**) show approximate transition zone between brittle sample edge and ductile sample volume.

4. Discussion

4.1. Hydrogen Absorption

The diffusivity and solubility of hydrogen is significantly different in the α and β phases. Hydrogen diffuses more into the β-phase, in which it has higher solubility due to this phase having more available interstitial sites (6 tetrahedral, 3 octahedral) in the bcc lattice than in the hexagonal close-packed (hcp) unit cell of the α-phase (2 tetrahedral, 1 octahedral) [22]. In the α-phase, the solubility of hydrogen is 0.08 wt% at the eutectoid temperature of 319 °C and it decreases with decreasing temperature [23]. On the other hand, the solubility of hydrogen in the β-phase is about five times higher at the eutectoid temperature, and considerably higher at its maximum solubility temperature of 640 °C (1.08 wt%) [23]. For this reason, alloys containing more β-phase are more sensitive to hydrogen penetration into the microstructure. At α/β interphase boundaries, hydrogen reacts with the α phase to form hydrides. These hydrides are of three types: δ-TiH_x with an fcc structure, ε-TiH with an fct or tetragonally distorted fcc structure ($c/a \leq 1$), and metastable γ-TiH type with an fct structure ($c/a > 1$) [14]. The degree of hydrogen-assisted degradation is determined by the mobility of hydrogen in the β-phase, temperature, pressure, and the size of grains, as well as other factors [24,25].

Hydrogen uptake depends heavily on the continuity of the β-phase. Generally, the rate of hydrogen diffusion is several orders of magnitude higher in the β-phase than in the α-phase. The observed difference in H concentration between the two-phase 3D + HT and CM samples can thus be first associated with their different microstructures [26]. A fully lamellar microstructure in the 3D + HT samples exhibits more continuous β-phase than the equiaxed microstructure of CM samples, with discontinuous β-phase at α-grain boundaries, and so higher H uptake can be expected [26]. Additionally, the depth of hydrogen ingress is logically much higher in the more continuous lamellar microstructure. Thus, three times the thickness of the affected layer was observed on optical micrographs (comparison between Figure 5e,h), as well as in the depth of hydride precipitation, as assessed by XRD (Figure 3b,c). Similarly, Navi et al. [14] proved a higher susceptibility to hydrogen embrittlement for PBF-EB/M manufactured Ti6Al-4V alloy compared to the wrought alloy, based on a more continuous network of β-phase lamellae. A lower lattice parameter of the β-phase (Figure 4) also contributes to a higher susceptibility to hydrogen embrittlement.

An interesting discrepancy occurs in case of 3D printed samples without heat treatment, which shows a fully martensitic structure. Although the hydrogen uptake in this study was undoubtedly the highest for the as-built 3D samples, Deconinck et al. [4], as well as Metalnikov et al. [18], reported lower hydrogen uptake compared to samples containing the β-phase. Kong et al. [27] explained that the lower hydrogen diffusion was caused by increased cellular dislocation structure. We attribute the highest H uptake to the high internal stresses associated with the martensitic microstructure formed during extremely rapid solidification intrinsic to the PBF-LB/M process. Capelle et al. [28] showed significant enhancement of hydrogen absorption due to present stresses in pipeline steels. Stresses also increased hydrogen uptake in tempered martensitic steel [29]. Motta et al. [30] reported stress to be an important factor for hydrogen influence in zirconium, which shows similar interactions with hydrogen to titanium.

4.2. Hydrogen Distribution in Ti-Al6-V4 Microstructure

Hydrogen distribution is highly dependent on the microstructure of Ti-6Al-4V alloy. Therefore, it is supposed to differ in all tested samples, as these show three different microstructure states: 1. fully martensitic (one-phase) acicular microstructure with high level of stresses in the as-built 3D sample, 2. lamellar α + β (two-phase) microstructure in the heat-treated 3D + HT sample, and 3. equiaxed α + β (two-phase) microstructure in the CM sample.

The 3D sample possesses a fully martensitic microstructure, as shown in Figure 6a and as analyzed thoroughly in other studies [31–33]. Such a structure, with a large degree of

internal stresses due to the rapid cooling during PBF-LB/M manufacturing, seems to be the most susceptible to hydrogen penetration under presented conditions. However, not many studies can be found discussing how hydrogen behaves in a fully martensitic material. Most probably, the H content in the hcp martensitic phase rapidly reaches the solubility limit, which leads to the precipitation of δ_A-hydride along with orthorhombic martensite α''. As hydrogen increases, the thermodynamic stability of the β-phase is altered and lowers the temperature of the reverse martensite transformation ($\alpha'' \rightarrow \beta$) down to room temperature at high enough concentrations (the hydrogen content reached more than 0.5 wt% in this sample, as presented in Table 2) [34]. The martensite transformed, to a large extent, into the β-phase (Figure 3a), capturing the most hydrogen entering the material. The significantly increased lattice parameter (Figure 4) testifies to hydrogen being predominantly dissolved in this phase. As the lattice parameter was invariant throughout the depth of the sample, we can assume that it concerns a new phase transformed due to hydrogen action, containing the maximum possible H concentration (H atoms filling nearly all interstitial sites). At the subsurface layer of the material, more hydrides were precipitated from the β_H-phase under ongoing H ingress (δ_B-hydride). The H-assisted phase transformations occurring at room temperature, being accompanied by large volumetric changes, explain the highly deformed microstructure shown in optical micrographs (Figure 5b,c).

A different reaction mechanism occurs in the case of a two-phase microstructure, which was present in 3D + HT and CM samples. Hydrogen preferentially diffuses through the β-phase with much higher hydrogen solubility and incorporates into the interstitial sites of the bcc solid solution, expanding its lattice parameter. In situ SEM with electron back-scattered diffraction (EBSD) in the study of Kim et al. [35] revealed that the lattice expansion of the hydrogenated β-phase introduces a localized stress field near the α/β phase boundary, which consequently induces hydrogen trapping in this region and facilitates heterogeneous hydride nucleation and growth along the boundary. With further hydrogen ingress, hydrides can eventually grow towards the α grain. Kim et al. [36] also pointed out the anisotropy in lattice expansion of the β_H-phase, with a gradual increase in the hydrogen concentration which might suggest a gradual displacive transformation of the β_H-phase into an fcc δ-hydride. This could explain the occurrence of the fcc δ_B-hydride determined in this study, mainly occurring in the subsurface layer, where the β_H-phase is highly saturated in H.

When a lamellar microstructure is present, α/β interfaces represent hydrogen diffusion channels rich in defects and provide ideal sites for hydride nucleation. In the equiaxed microstructure, hydrides can more easily precipitate inside the α-phase as the hydrogen saturation in the α-phase is much lower than that in β-phase [37]. This is supported by [26], where micro-cracks associated with hydrogen embrittlement were located mainly in the equiaxed grains of primary α.

Tal-Gutelmacher and Eliezer [26] also proved that hydride precipitation occurs at lower hydrogen concentrations in a discontinuous equiaxed microstructure due to the lower H solubility in the α-phase. This explains similar phase concentration profiles in both 3D and CM samples (Figure 3), despite the difference in the analyzed H concentrations (Table 2). Even so, slightly less hydrides were present in the CM samples.

Compared to PBF-EB/M samples studied by Navi et al. [14], no cracks or microvoids were observed in the microstructure of the hydrogen-charged samples prepared using PBF-LB/M. This difference points to the dissimilar behavior of materials prepared using different 3D printing technologies. PBF-EB/M-manufactured Ti alloy seems to be more prone to H-assisted cracking due to the presence of a continuous network of β-phase at the boundaries of prior β-grains.

4.3. Hydrides

Despite different preparation routes and different microstructures in the three studied samples of Ti-6Al-4V alloy, the XRD analysis confirmed the presence of the same hydrides for all samples. Due to the high similarity to the results obtained by Navi et al. [14] (elec-

trochemically charged Ti-6Al-4V alloy prepared via PBF-EB/M additive manufacturing) and subsequently by Wu et al. [3] (electrochemically charged Ti-6Al-4V alloy prepared via PBF-LB/M), we designated the present hydrides in the same way as in [14], δ_A- and δ_B-hydride, although the lattice parameters and assigned lattice type are not the same. The peaks associated with such hydrides can be identified with the peaks we assigned to the hydrides present in our study. Different 2-theta angles are due to the use of Cu-radiation compared to the Co-radiation used in this study. However, while Navi et al. [14] observed two types of fcc hydrides, a thorough Rietveld refinement applied in this study and supported by the theoretical results of Wang and Wang [21] showed the δ_A-hydride was better fitted to a tetragonal (fct) hydride. Similarly, Kim et al. [35] used the predicted ab initio calculations from [21] to better fit the obtained XRD patterns and stated that the metastable fct TiH1.5 hydride is the dominant phase formed by hydrogenation at room temperature. Phase fitting, which managed to assign all peaks with a very good fit, is shown in a Supplementary File in Figure S1. Nevertheless, reliable determination of the present hydrides would require more sophisticated and complex methods of characterization.

4.4. Influence of Hydrogen on Mechanical Properties

The microhardness profiles in Figure 7 clearly illustrate the distinct effects of hydrogen on the studied materials. These differences highlight the varying impacts of hydrogen within different microstructural states of the Ti-Al6-V4 alloy. The conventionally manufactured sample (Figure 7c) has shown a clear hardness increase in the surface layer, measuring about 150 μm. This level of depth approximately corresponds with the depth of the visually affected layer observed in optical micrographs (~110 μm, Figure 5h,i), as well as the depth in which hydrides dominate (Figure 3c). The observed hardness increase can be related to the growth of internal stresses in the material due to the dissolution of hydrogen in the α and β solid solutions and distortion of the crystal lattice by formation of hydrides [10,35]. The as-built 3D printed sample behaved in the opposite manner (Figure 7a), but the hardness profile can also be accurately related to the microstructural changes. The hardness of the core material exponentially dropped towards the sample surface. The original hardness value stabilized at a depth of approximately 500 μm. This depth corresponds well with the depth of the visually affected surface layer in the optical micrographs (Figure 5b,c). The hardness drop can be related to the release of high internal stresses trapped in the original as-built material with metastable martensitic microstructure via hydrogen-assisted transformation into stable (and softer) β_H-phase, and the precipitation of hydrides (Figure 3a). The effect of the β-phase on mechanical behavior is also visible in the lower elastic stiffness of this material. After the heat treatment, the influence of hydrogen on material hardness was subdued (Figure 7b). Similarly to the CM sample, hydrogen influenced material hardness in a positive way. However, due to the different microstructure of a lamellar type (Figure 6d), most hydrogen diffused through lamellae of the β-phase and precipitated into δ_A-TiH1.5 hydrides on the α/β phase interfaces predominantly. The hardening effect of such hydrides is much weaker than that of those precipitated inside the equiaxed α grains. Peak hardness at a depth of 100–150 μm agrees with the observed increase in the content of both hydrides (Figure 3b). The microhardness of the superficial layer is weakened by approximately double the amount of β-phase as compared to the original state.

A strong reduction in strength and ductility was observed for all types of samples as a result of hydrogen charging (Figure 8). The most severe decrease in strength and a complete loss of ductility in the case of the as-built sample without heat treatment can be primarily attributed to the highest H content after H-charging (Table 2), and secondly to the release of high residual stresses by the partial change of the nonequilibrium fully martensitic structure to β_H with hydrides (Figure 2). The change in UTS (50% drop) for the 3D-printed sample with heat treatment was not as severe as for the sample without heat treatment (85% drop) because it preserved its original two-phase lamellar microstructure (Figure 6f). Both 3D-printed samples exhibited a shift towards brittleness due to the introduction of hydrogen. However, upon examination of the fractographic characteristics

(as depicted in Figure 9b,d), the brittleness primarily manifested in the subsurface layer of the samples. Although the performed analyses have confirmed the hydrogen effect throughout the sample volume, this effect within the core region did not impede the material's capacity for plastic deformation; in the sample core, the presence of hydrides limiting ductility constituted merely 4–8 vol% (Figure 3a,b) and the partial replacement of the martensitic phase by the β_H-phase (3D_H sample, Figure 3a) is expected to have a beneficial contribution to local ductility. However, as the ductile core constituted less than 50% of the sample cross-section, the macroscopic behavior of the samples controlled by the extensive brittle subsurface area was brittle. The conventionally manufactured sample preserved its strength and partially even its ductility. The discontinuity of the β-phase in the equiaxed microstructure (Figure 6g) reduced the hydrogen uptake and the depth of hydrogen penetration. Most hydrogen thus remained in the relatively narrow surface layer of the samples compared to other samples (about 250 μm; Figures 3c and 4), and it did not significantly affect the remaining volume of the samples (est. 87%). Therefore, some ductility was retained.

4.5. Effect of Heat Treatment

Different outcomes regarding the influence of heat treatment on sensitivity to hydrogen embrittlement than reported in the study of Kong et al. [27] can be explained by a very different state of H-charging. The microstructure with more β-phase after higher T annealing contained only 100 ppm of H compared to 3772 ppm in our work. As-built stress-relieved samples contained about 40 ppm only. Under such conditions, all H was trapped reversibly. Although some hydrides were detected in the heat-treated H-charged samples by XRD, transmission electron microscopy (TEM) and EBSD, these were most probably initiated at α/β interfaces by straining (reported strain of 3%). Otherwise, all H in this content is supposed to be dissolved in the β solid solution. The conclusion that heat-treated samples show a decreased resistance against hydrogen embrittlement is thus valid only under such mild H influence. The decrease in the mechanical performance of heat-treated samples compared to as-built samples observed in [27] is disputable.

5. Conclusions

The examination of the 3D-printed Ti-Al6-V4 alloy in both its as-built and annealed states, compared with the conventionally manufactured alloy, revealed notable differences in hydrogen uptake under equivalent charging conditions. The primary factor driving this disparity is the difference in the continuity of the microstructure. Otherwise, all the tested materials showed the presence of identical hydrides, indicating that the interaction between hydrogen and the material remains unchanged; what differs is the reaction mechanism and distribution of hydrogen (and hydrides consequently) in particular microstructures.

Distinctive behavior is exhibited by the as-built state of the 3D-printed Ti-Al6-V4 alloy, characterized by a fully martensitic microstructure with high residual stresses after extremely rapid solidification during PBF-LB/M. In this structure, hydrogen has been shown to aggressively penetrate the material and transform the metastable martensite into the β-phase. Such newly formed solid solution of hydrogen in β_H-phase was characterized by 10% larger volume of the bcc unit cell compared to the β-phase present in the original 3D-printed alloy after heat treatment.

High concentrations of H and H penetration through the entire cross-section in the 3D-printed samples led to the shift towards brittleness. The hydrogen influence in conventionally manufactured samples was confined mainly to the surface layer of the samples, and while it also resulted in a decline in mechanical performance, the yield strength experienced minimal alteration, and the samples partially retained the ability of plastic deformation.

In practical terms, it is essential to acknowledge the increased susceptibility to hydrogen embrittlement when handling PBF-LB/M-printed products made of Ti-Al6-V4 alloy. Employing heat treatment has not been shown to be an effective tool for preventing hydro-

gen embrittlement. Although about 30% less hydrogen was absorbed, only the adverse effect of hydrogenation on sample strength was mitigated.

Supplementary Materials: The following supporting information can be downloaded at: https://www.mdpi.com/article/10.3390/met14020251/s1, Figure S1: Phase fitting applied in the XRD analysis of the tested materials.

Author Contributions: Conceptualization, D.V. and M.R.; methodology, Z.K., M.R., J.D. and D.V.; investigation, Z.K., M.R., D.D. and J.D.; resources, D.V.; data curation, M.R., D.D. and J.D.; writing—original draft preparation, M.R., J.D. and Z.K.; writing—review and editing, D.D. and D.V.; supervision, D.V.; funding acquisition, D.V. All authors have read and agreed to the published version of the manuscript.

Funding: This research was funded by the Ministry of Education, Youth and Sports, grant for specific university research A1_FCHT_2023_009.

Data Availability Statement: The raw data supporting the conclusions of this article will be made available by the authors on request.

Acknowledgments: We acknowledge Ondrej Ekrt (Institute of Physics, Czech Academy of Sciences) for providing the combustion analysis.

Conflicts of Interest: The authors declare no conflicts of interest. The funders had no role in the design of the study; in the collection, analyses, or interpretation of data; in the writing of the manuscript; or in the decision to publish the results.

References

1. Nguyen, H.D.; Pramanik, A.; Basak, A.K.; Dong, Y.; Prakash, C.; Debnath, S.; Shankar, S.; Jawahir, I.S.; Dixit, S.; Buddhi, D. A critical review on additive manufacturing of Ti-6Al-4V alloy: Microstructure and mechanical properties. *J. Mater. Res. Technol.* **2022**, *18*, 4641–4661. [CrossRef]
2. Kudiiarov, V.N.; Syrtanov, M.S.; Bordulev, Y.S.; Babikhina, M.N.; Lider, A.M.; Gubin, V.E.; Murashkina, T.L. The hydrogen sorption and desorption behavior in spherical powder of pure titanium used for additive manufacturing. *Int. J. Hydrogen Energy* **2017**, *42*, 15283–15289. [CrossRef]
3. Wu, W.; He, G.; Huang, J.; Zhang, A.; Liu, X.; Ouyang, Z.; Sun, Z.; Guan, L.; Chu, S.; Li, P.; et al. Influence of electrochemically charged hydrogen on mechanical properties of Ti–6Al–4V alloy additively manufactured by laser powder-bed fusion (L-PBF) process. *Mater. Sci. Eng. A* **2023**, *866*, 144339. [CrossRef]
4. Deconinck, L.; Bernardo Quejido, E.; Villa Vidaller, M.T.; Jägle, E.A.; Verbeken, K.; Depover, T. The mechanism behind the effect of building orientation and surface roughness on hydrogen embrittlement of laser powder bed fused Ti-6Al-4V. *Addit. Manuf.* **2023**, *72*, 103613. [CrossRef]
5. Dwivedi, S.K.; Vishwakarma, M. Hydrogen embrittlement in different materials: A review. *Int. J. Hydrogen Energy* **2018**, *43*, 21603–21616. [CrossRef]
6. Tal-Gutelmacher, E.; Eliezer, D. The hydrogen embrittlement of titanium-based alloys. *JOM* **2005**, *57*, 46–49. [CrossRef]
7. Liu, Z.; Zhao, D.; Wang, P.; Yan, M.; Yang, C.; Chen, Z.; Lu, J.; Lu, Z. Additive manufacturing of metals: Microstructure evolution and multistage control. *J. Mater. Sci. Technol.* **2022**, *100*, 224–236. [CrossRef]
8. Liović, D.; Franulović, M.; Kozak, D. The effect of process parameters on mechanical behavior of selective laser melted Ti6Al4V alloy. *Procedia Struct. Integr.* **2023**, *46*, 42–48. [CrossRef]
9. Jamhari, F.I.; Foudzi, F.M.; Buhairi, M.A.; Sulong, A.B.; Mohd Radzuan, N.A.; Muhamad, N.; Mohamed, I.F.; Jamadon, N.H.; Tan, K.S. Influence of heat treatment parameters on microstructure and mechanical performance of titanium alloy in LPBF: A brief review. *J. Mater. Res. Technol.* **2023**, *24*, 4091–4110. [CrossRef]
10. Laptev, R.; Kudiiarov, V.; Pushilina, N. Hydrogen influence on defect structure and mechanical properties of EBM Ti-6Al-4V. *Mater. Today Proc.* **2019**, *19*, 2084–2088. [CrossRef]
11. Pushilina, N.; Panin, A.; Syrtanov, M.; Kashkarov, E.; Kudiiarov, V.; Perevalova, O.; Laptev, R.; Lider, A.; Koptyug, A. Hydrogen-Induced Phase Transformation and Microstructure Evolution for Ti-6Al-4V Parts Produced by Electron Beam Melting. *Metals* **2018**, *8*, 301. [CrossRef]
12. Pushilina, N.; Syrtanov, M.; Kashkarov, E.; Murashkina, T.; Kudiiarov, V.; Laptev, R.; Lider, A.; Koptyug, A. Influence of Manufacturing Parameters on Microstructure and Hydrogen Sorption Behavior of Electron Beam Melted Titanium Ti-6Al-4V Alloy. *Materials* **2018**, *11*, 763. [CrossRef]
13. Metalnikov, P.; Eliezer, D.; Ben-Hamu, G.; Tal-Gutelmacher, E.; Gelbstein, Y.; Munteanu, C. Hydrogen embrittlement of electron beam melted Ti–6Al–4V. *J. Mater. Res. Technol.* **2020**, *9*, 16126–16134. [CrossRef]

14. Navi, N.U.; Tenenbaum, J.; Sabatani, E.; Kimmel, G.; Ben David, R.; Rosen, B.A.; Barkay, Z.; Ezersky, V.; Tiferet, E.; Ganor, Y.I.; et al. Hydrogen effects on electrochemically charged additive manufactured by electron beam melting (EBM) and wrought Ti–6Al–4V alloys. *Int. J. Hydrogen Energy* **2020**, *45*, 25523–25540. [CrossRef]
15. Bilgin, G.M.; Esen, Z.; Akın, Ş.K.; Dericioglu, A.F. Optimization of the mechanical properties of Ti-6Al-4V alloy fabricated by selective laser melting using thermohydrogen processes. *Mater. Sci. Eng. A* **2017**, *700*, 574–582. [CrossRef]
16. Guo, Y.; Fang, Y.; Dai, G.; Sun, Z.; Wang, Y.; Yuan, Q. The effect of hydrogen treatment on microstructures evolution and mechanical properties of titanium alloy fabricated by selective laser melting. *J. Alloys Compd.* **2022**, *890*, 161642. [CrossRef]
17. Silverstein, R.; Eliezer, D. Hydrogen trapping in 3D-printed (additive manufactured) Ti-6Al-4V. *Mater. Charact.* **2018**, *144*, 297–304. [CrossRef]
18. Metalnikov, P.; Eliezer, D.; Ben-Hamu, G. Hydrogen trapping in additive manufactured Ti–6Al–4V alloy. *Mater. Sci. Eng. A* **2021**, *811*, 141050. [CrossRef]
19. Kacenka, Z.; Roudnicka, M.; Ekrt, O.; Vojtech, D. High susceptibility of 3D-printed Ti-6Al-4V alloy to hydrogen trapping and embrittlement. *Mater. Lett.* **2021**, *301*, 130334. [CrossRef]
20. Rietveld, H.M. A profile refinement method for nuclear and magnetic structures. *J. Appl. Crystallogr.* **1969**, *2*, 65–71. [CrossRef]
21. Wang, X.-Q.; Wang, J.-T. Structural stability and hydrogen diffusion in TiHx alloys. *Solid State Commun.* **2010**, *150*, 1715–1718. [CrossRef]
22. AZO Materials. Available online: http://www.azom.com/article.aspx?ArticleID=1341#_Tensile_Strength (accessed on 6 January 2023).
23. Wille, G.; Davis, J. *Hydrogen in Titanium Alloys*; McDonnell Douglas Astronautics, Co.: St. Louis, MO, USA, 1981.
24. Stepanova, E.; Pushilina, N.; Syrtanov, M.; Laptev, R.; Kashkarov, E. Hydrogen effect on Ti-6.5Al-3.5Mo-1.5Zr-0.3Si parts produced by electron beam melting. *Int. J. Hydrogen Energy* **2019**, *44*, 29380–29388. [CrossRef]
25. Eliezer, D.; Tal-Gutelmacher, E.; Cross, C.E.; Boellinghaus, T. Hydrogen absorption and desorption in a duplex-annealed Ti–6Al–4V alloy during exposure to different hydrogen-containing environments. *Mater. Sci. Eng. A* **2006**, *433*, 298–304. [CrossRef]
26. Tal-Gutelmacher, E.; Eliezer, D. High fugacity hydrogen effects at room temperature in titanium based alloys. *J. Alloys Compd.* **2005**, *404–406*, 613–616. [CrossRef]
27. Kong, D.; Zhao, D.; Zhu, G.; Ni, X.; Zhang, L.; Wu, W.; Man, C.; Zhou, Y.; Dong, C.; Sun, B. Heat treatment effects on the hydrogen embrittlement of Ti6Al4V fabricated by laser beam powder bed fusion. *Addit. Manuf.* **2022**, *50*, 102580. [CrossRef]
28. Capelle, J.; Dmytrakh, I.; Pluvinage, G. Comparative assessment of electrochemical hydrogen absorption by pipeline steels with different strength. *Corros. Sci.* **2010**, *52*, 1554–1559. [CrossRef]
29. Masuda, Y.; Koyama, M.; Kakinuma, H.; Akiyama, E. Mechanical loading effect on the hydrogen uptake of tempered martensite steel: Elastic strain effect vs. plastic strain effect. *Mater. Sci. Eng. A* **2023**, *862*, 144486. [CrossRef]
30. Motta, A.T.; Capolungo, L.; Chen, L.-Q.; Cinbiz, M.N.; Daymond, M.R.; Koss, D.A.; Lacroix, E.; Pastore, G.; Simon, P.-C.A.; Tonks, M.R.; et al. Hydrogen in zirconium alloys: A review. *J. Nucl. Mater.* **2019**, *518*, 440–460. [CrossRef]
31. Fousova, M.; Vojtech, D. Thermal treatment of 3D-printed Titanium alloy. *Manuf. Technol.* **2018**, *18*, 227–232. [CrossRef]
32. Yang, J.; Yu, H.; Yin, J.; Gao, M.; Wang, Z.; Zeng, X. Formation and control of martensite in Ti-6Al-4V alloy produced by selective laser melting. *Mater. Des.* **2016**, *108*, 308–318. [CrossRef]
33. Motyka, M. Martensite Formation and Decomposition during Traditional and AM Processing of Two-Phase Titanium Alloys—An Overview. *Metals* **2021**, *11*, 481. [CrossRef]
34. Ilyin, A.A.; Kollerov, M.Y.; Mamonov, A.M.; Krastilevsky, A.A.; Makarenkov, D.Y. Hydrogen Influence on Martensitic Transformation and Shape Memory Effect in Titanium Alloys. *J. Phys. IV France* **1995**, *5*, C8-1145–C8-1150. [CrossRef]
35. Kim, J.; Plancher, E.; Tasan, C.C. Hydrogenation-induced lattice expansion and its effects on hydrogen diffusion and damage in Ti–6Al–4V. *Acta Mater.* **2020**, *188*, 686–696. [CrossRef]
36. Kim, J.; Kang, J.; Tasan, C.C. Hydride formation in Ti6Al4V: An in situ synchrotron X-ray diffraction study. *Scr. Mater.* **2021**, *193*, 12–16. [CrossRef]
37. Liu, H.J.; Zhou, L.; Liu, P.; Liu, Q.W. Microstructural evolution and hydride precipitation mechanism in hydrogenated Ti–6Al–4V alloy. *Int. J. Hydrogen Energy* **2009**, *34*, 9596–9602. [CrossRef]